JCTC Journal of Chemical Theory and Computation

pubs.acs.org/JCTC Article

An Implicit-Solvent Model for the Interfacial Configuration of Colloidal Nanoparticles and Application to the Self-Assembly of Truncated Cubes

U. Gupta and F. A. Escobedo*

Cite This: J. Chem. Theory Comput. 2020, 16, 5866−5875 Read Online

ACCESS | Metrics & More | Article Recommendations | Supporting Information

ABSTRACT: This study outlines the development of an implicit-solvent model that reproduces the behavior of colloidal nanoparticles at a fluid−fluid interface. The center point of this formulation is the generalized quaternion-based orientational constraint (QOCO) method. The model captures three major energetic characteristics that define the nanoparticle configuration—position (orthogonal to the interfacial plane), orientation, and inter-nanoparticle interaction. The framework encodes physically relevant parameters that provide an intuitive means to simulate a broad spectrum of interfacial conditions. Results show that for a wide range of shapes, our model is able to replicate the behavior of an isolated nanoparticle at an explicit fluid−fluid interface, both qualitatively and often nearly quantitatively. Furthermore, the family of truncated cubes is used as a test bed to analyze the effect of changes in the degree of truncation on the potential-of-mean-force landscape. Finally, our results for the self-assembly of an array of cuboctahedra provide corroboration to the experimentally observed honeycomb and square lattices.

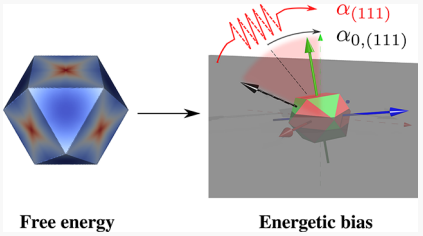

1. INTRODUCTION

The presence of a fluid−fluid interface imposes certain restrictions on the position and orientation of a nanoparticle (NP) that resides across or in close proximity to the interface-dividing plane. This effect has been exploited to create long-range, coherent assemblies of quasi-2D superstructures. These structures are of particular interest because they are known to possess strong correlations between their packing symmetries (structure) and the displayed opto-electronic properties (function). In particular, different NP shapes display a gamut of orientation behavior depending on the interfacial conditions. Multiple experimental[1−4] and computational[5−12] studies, reported over the recent years, have aimed to develop a finer control over NP interfacial assembly. However, most of these computational studies have primarily focused on single-particle behavior due to the high computational demands entailed in simulating the surrounding fluids and the resulting interface. This limitation prevents extensive computational examination of the mechanism and energetics of the self-assembly process that leads to the formation of superlattices possessing atomic coherence across micrometer-sized grains.[13] To help fill in this gap, we put forth a theoretical framework, backed by explicit-solvent simulation studies,[11] that accounts for the effect of the fluid−fluid interface on the NP using an effective overlaid potential landscape. By eliminating the explicitly modeled solvent molecules in favor of an implicit solvent, the number of particles to be simulated is greatly reduced. The associated reduction in computational expenses allows access to the self-assembly process at meso-length scales ($O(10^3)$ the size of a representative NP). Moreover, due to the high dimensional nature of the possible control parameters and conditions, a large portion of this phase space remains unexplored. In this context, implicit-solvent simulations can provide an effective means for exploration of a wide range of interfacial conditions (determined by the choice of solvents), NP choice (shapes and sizes), and even meso-scale phenomena observed experimentally (like defects and grain boundaries).

In a previous work,[11] we chose intrinsic ($y - z' - y''$ coordinate convention) Euler angles (ϕ, θ, ψ) to describe the NP orientation. The advantage of this representation lies in the isolation of the rotation about the global axis perpendicular to the interface (ϕ). Since transformations around ϕ produce no change in the NP orientation with respect to the interface, ϕ can be factored out by leveraging the intrinsic cylindrical symmetry about the interface normal. Direct application of the above idea requires two independent springs to constrain the θ and ψ rotations as reported by Soligno and Vanmaekelbergh.[12] However, the Euler angle formulation suffers from operational difficulties such as the gimbal lock,[14] leading to discontinuities at the poles ($\theta = 0, \pi$). More importantly, analysis of the free-energy (FE) plots for a range of NP shapes from explicit-solvent simulations points to an underlying symmetry in the orientation characteristics. We posit that the overall orientation bias

Received: March 24, 2020
Published: July 27, 2020

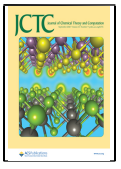

https://dx.doi.org/10.1021/acs.jctc.0c00283
J. Chem. Theory Comput. 2020, 16, 5866−5875

function can be broken down into the sum of contributions from individual particle shape features. Each feature therein corresponds to a hypothetical (hkl) NP facet and comprises a basis set. Here, an (hkl) facet represents (the miller indices of) a crystallographic plane. It is important to note that the "biases" applied to an NP in the implicit-solvent simulations are intended to recreate the effect of the interface on the NP (orientation and vertical position) behavior. These biases should not be confused with those employed for the purpose of facilitating sampling (like non-Boltzmann sampling).

We propose a generalized formulation based on generating a potential-of-mean-force (PMF) function by superimposing the orientation constraints for multiple relevant NP features. Although all of the possible (hkl) features are relevant, some contribute much more to the free-energy landscape. In this context, the formulation of the orientation bias is analogous to a Fourier series expansion with leading terms dominating local behavior. Individual constraints [for each (hkl) feature] are generated using the quaternion-based orientational constraint (QOCO) method. The QOCO method is predicated on three major known priors of the physical system. First, it enforces rotational invariance about the global vertical axis to replicate the cylindrical symmetry of the interface. Second, owing to a quaternion implementation, any generated torque is a continuous function across the entire rotation space. Lastly, it factors out the equivalent orientations in rotationally symmetric polyhedra.

In section 2, we outline the details of our heuristic formulation and the QOCO method. In section 3.1, we demonstrate the ability of the formulation to capture the orientation characteristics of a wide range of polyhedral shapes using single- and multiple-feature biases. Thereafter, in section 3.2, we explore the underlying physical basis of the generated model parameterization. We focus on two separate cases to justify our design choices and to provide concrete examples for the parameter set. First, we consider cantellated cubes with {110} and {111} facet truncations, ranging from a cube (CU) to the rhombicuboctahedron (RCO). Then, we consider the series of {111} facet truncations from a cuboctahedron (CO) to the truncated octahedron (TO). We then discuss the geometric and energetic basis for the dominant contribution from certain features. Having established a physical correlation, we use the model to analyze the effect of changes in NP shape on the orientation characteristics. In section 3.3, we present preliminary results for the self-assembly of an array of CO NPs (size of ∼5 nm) at three different interfacial conditions. To this end, a large number of coarse-grained polybead NPs are simulated in a highly parallelized molecular dynamics (MD) setting.[11] In agreement with experiments,[7,15−18] we observe the formation of bilayer honeycomb and monolayer square lattices. Lastly, in section 4, we provide some concluding remarks and comments on potential limitations and extensions of our approach.

2. MODEL

We consider a biasing potential to describe the effective interaction between the NP and the two fluids forming the interface. The total bias applied to each NP, with shape S, is given by

$$E_b(S, H, \vec{\mathbf{q}}) = E_v(S, H, \vec{\mathbf{q}}) + E_t(S, \vec{\mathbf{q}}) \tag{1}$$

where H is the vertical position of the NP center-of-mass from the interfacial plane, and the quaternion $\vec{\mathbf{q}}$ defines the orientation of the NP from a fixed, arbitrary reference.

2.1. Choice of the Bias Functions. The component biases, vertical position (E_v) and orientation (E_t), are described as follows.

1. Vertical position bias, E_v: Due to the non-negligible interfacial mixing region[11] and thermal energy, the NP vertical position is expected to fluctuate significantly about the interfacial plane. This characteristic can be captured by tethering the NP to the interfacial plane (at $y = 0$) using a spring.[12] The harmonic potential, E_v, is given as

$$E_v(S, H, \vec{\mathbf{q}}) = g(S, H, \vec{\mathbf{q}})\frac{k_v'}{2}H^2 = \frac{k_v}{2}H^2 \tag{2}$$

Typically, the orientation and vertical position of the NP at the interface are correlated. Previously, we have shown that as the NP moves away from the interfacial plane, the orientation preference changes. For the sake of simplicity, we currently do not take this effect into account and hence set the function $g(S, H, \vec{\mathbf{q}})$ as constant, thereby making the E_v and E_t biases independent. The parameter k_v is extracted from the explicit-solvent simulation results reported in ref 11 by fitting a parabola to the FE plot [Figure 1a]. For example, for an RCO of edge length $e = 4\sigma$, $k_v = 3.8\frac{k_BT}{\sigma^2}$. Choosing this form of the harmonic potential imposes a quasi-2D confinement on the NPs. The infinitely deep well is convenient for simulations as it prevents the desorption of NPs from the interface. If needed, a different functional form can be used to more closely reproduce the flat FE profile far from the interfacial plane, e.g., a harmonic potential with a switchover to a constant value beyond an |H| cutoff, or a Gaussian (akin to eq 3b below).
2. Orientation bias, E_t: The total orientation bias is defined as a linear superposition of the single-feature potentials, $E_{t,f}$

$$E_t(S, \vec{\mathbf{q}}) = \sum_{f \in F_S} E_{t,f} \tag{3}$$

Similar to the vertical position bias, the form of the single-feature potential could be harmonic

$$E_{t,f} = \frac{1}{2}k_{t,f}(\alpha_{m,f}(\vec{\mathbf{q}}) - \alpha_{0,f})^2 \tag{3a}$$

where $k_{t,f}$ is the spring constant, $\alpha_{m,f}(\vec{\mathbf{q}})$ is defined as the angle of closest approach, and $\alpha_{0,f}$ is the equilibrium angle (see details below).

We also consider a Gaussian form, with an additional parameter, which has the advantage that the width (σ_f) and depth (ϵ_f) of the potential well can be controlled independently

$$E_{t,f} = -k_{t,f}{\sigma_f}^2 \exp\left(\frac{-(\alpha_{m,f}(\vec{\mathbf{q}}) - \alpha_{0,f})^2}{2{\sigma_f}^2}\right) = -\epsilon_f \exp\left(\frac{-\Delta{\alpha_{m,f}}^2}{2\sigma_f^2}\right) \tag{3b}$$

The feature space, F, is composed of all possible (hkl) planes. In general, an (hkl) orientation implies that the (hkl) facet is oriented parallel to the interface normal (i.e., facing vertically upward). Each single-feature potential,

https://dx.doi.org/10.1021/acs.jctc.0c00283
J. Chem. Theory Comput. 2020, 16, 5866−5875

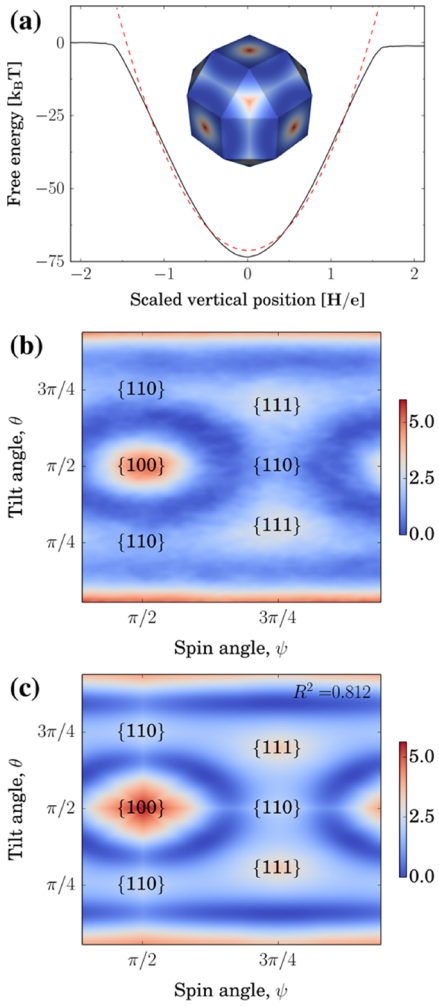

Figure 1. Interfacial explicit- and implicit-solvent model for RCO (edge size $e = 4\sigma$). (a) Comparison of the single-NP vertical FE from the explicit-solvent calculations (black, solid) and the fitted parabola (red, dotted) of the implicit-solvent model. (b,c) FE (k_BT units in the color bars) as a function of orientation (θ, ψ), from explicit-solvent calculations compared to a fitted 2-feature {100},{111} Gaussian bias model. The bias is plotted on the surface of the RCO in the inset of a.

$E_{t,\,(hkl)}$, adds a tendency to point the corresponding (hkl) facet at an angle $\alpha_{0,\,(hkl)}$ from the vertical. However, depending on the application, only a subset F_S, defined by the NP shape (S), may be relevant. For the family of truncated cubes under consideration, choosing the subset, $F_S \subseteq \{\{111\}, \{110\}, \{100\}\}$ is sufficient. The basis functions, $\alpha_{m,\,(hkl)}(\vec{\mathbf{q}})$, capture the orientation of their corresponding NP facets relative to the interface normal and are calculated using the QOCO method (described in the following section). The corresponding model parameters ($k_{t,\,f}$, $\alpha_{0,\,f}$, and σ_f) are obtained by fitting the bias function, $E_t(S, \vec{\mathbf{q}})$, to explicit-solvent FE results[11] [e.g., Figure 1b,c for an RCO ($e = 4\sigma$)] and are reported in Table 1.

The physical significance of parameters $k_{t,f}$ and k_v is discussed in section 3.

We report results for conditions corresponding to symmetric interactions between the NP and the two fluids forming the interface. Accordingly, the respective contact angle values (between the NP surface and each fluid) are close to 90°.[11,19]

Table 1. Parameter Sets for Orientation Bias for the Representative NP Shapes[a]

		Gaussian (single feature)					Gaussian (2 features)						harmonic (2 features)				
polyhedron	edge (σ)	$\{hkl\}$	$\alpha_{0,\,\{hkl\}}$	$k_{t,\,\{hkl\}}$	$\sigma_{\{hkl\}}$	R_S^2	R^2	$\{hkl\}$	$\alpha_{0,\,\{hkl\}}$	$k_{t,\,\{hkl\}}$	$\sigma_{\{hkl\}}$	R_S^2	R^2	$\{hkl\}$	$\alpha_{0,\,\{hkl\}}$	$k_{t,\,\{hkl\}}$	R_S^2	R^2
cube (CU)	5	100	54.7°	44.6	31.8°	0.98	0.96	100	52.3°	55.9	29.8°	0.98	0.97	100	54.7°	27.8	0.96	0.96
								110	45.0°	9.0	32.3°			110	45.0	5.8		
rhombicuboctahedron (RCO)	4	100	31.2°	118.0	10.7°		0.65	100	29.4°	128.9	7.07°		0.81	100	29.8°	41.0		0.74
								111	22.0°	24.1	50.0°			111	0	5.2		
cuboctahedron (CO)	5	111	0	80.0	19.5°	0.94	0.90	111	5.35°	58.1	24.4°	0.94	0.92	111	0	28.6	0.91	0.81
								110	45.0°	27.0	15.0°			110	45°	17.7		
truncated octahedron (TO)	4	110	45°	124.1	14.7°	0.86	0.78	111	54.7°	6.8	50.6°	0.86	0.84	111	54.7°	11.2	0.78	0.67
								110	45°	87.1	17.7°			110	45°	36.6		

[a]The goodness-of-fit is reported in terms of the coefficient of determination by matching orientation basins centered about {100}, {110}, and {111} (R_S^2) and the entire landscape (R^2). The spring constant, k_t values ($\frac{k_BT}{rad^2}$), equilibrium angle, α_0 (degrees), and standard of deviation, σ (degrees) are reported corresponding to the R^2 fits. The R_S^2 values are also reported for a different fit (different parameter set).

https://dx.doi.org/10.1021/acs.jctc.0c00283
J. Chem. Theory Comput. 2020, 16, 5866−5875

However, the model is general and should be applicable to cases with disparate fluid-NP contact angles.

2.2. Quaternion-Based Orientational Constraint. Quaternions represent a rotation between any two orientations in 3D space. Instead of performing a series of rotations about the principal axes attached to the NP, the transformation between the two orientations can be described by one rotation about a specific, global axis. Quaternions also represent orientations in terms of a rotation from some reference quaternion [typically the identity quaternion, (1,0,0,0)]. Let $\vec{\mathbf{q}}_{\mathbf{f}=(hkl)}$ be a general NP orientation with the (hkl) facet pointing vertically upward. The angle of closest approach, $\alpha_{m,f}$, is defined as the minimum angle of rotation between the current orientation, $\vec{\mathbf{q}}$, and the feature orientation, $\vec{\mathbf{q}}_{\mathbf{f}}$, while accounting for the rotational symmetries of the shape. The method [illustrated in section I of the Supporting Information] can be broken down into two sequential steps:

2.2.1. Conversion to the Axis-Angle Representation. In terms of the intrinsic Euler angles, an orientation quaternion, $\vec{\mathbf{q}}$ can be defined as a composition of three subsequent rotations

$$\vec{\mathbf{q}}(\phi, \theta, \psi) = \vec{\mathbf{q}}_{\phi}\vec{\mathbf{q}}_{\theta}\vec{\mathbf{q}}_{\psi} = \begin{bmatrix} \cos\left(\frac{\phi}{2}\right) \\ 0 \\ \sin\left(\frac{\phi}{2}\right) \\ 0 \end{bmatrix} \begin{bmatrix} \cos\left(\frac{\theta}{2}\right) \\ 0 \\ 0 \\ \sin\left(\frac{\theta}{2}\right) \end{bmatrix} \begin{bmatrix} \cos\left(\frac{\psi}{2}\right) \\ 0 \\ \sin\left(\frac{\psi}{2}\right) \\ 0 \end{bmatrix} \tag{4}$$

The rotation from the current orientation $\vec{\mathbf{q}}(\phi, \theta, \psi)$ to the feature orientation $\vec{\mathbf{q}}_{\mathbf{f}}(\phi_f, \theta_f, \psi_f)$ can be defined using a unit quaternion, $\vec{\mathbf{d}}_{\mathbf{f}}$, in the axis-angle representation, as

$$\vec{\mathbf{d}}_{\mathbf{f}} = \vec{\mathbf{q}}_{\mathbf{f}}\,\vec{\mathbf{q}}^{-1} = \cos\left(\frac{\alpha_f}{2}\right) + \sin\left(\frac{\alpha_f}{2}\right)\hat{\mathbf{r}}_{\mathbf{f}} = d_{r,f} + d_{i,f}\hat{\mathbf{i}} + d_{j,f}\hat{\mathbf{j}} + d_{k,f}\hat{\mathbf{k}} \tag{5}$$

where α_f is the angle of rotation about the unit vector $\hat{\mathbf{r}}_{\mathbf{f}}(= u\hat{\mathbf{i}} + v\hat{\mathbf{j}} + w\hat{\mathbf{k}})$ representing the axis of rotation. An important part of the method is to include the effect of cylindrical symmetry at the interface by enforcing rotational invariance about the global vertical axis. Since ϕ represents a rotation about the global vertical axis, the transformation due to $\vec{\mathbf{d}}_{\mathbf{f}}$ should leave ϕ unchanged. It can be shown that for $\phi_f = \phi$

$$\alpha_f = p(\vec{\mathbf{q}}, \vec{\mathbf{q}}_{\mathbf{f}}) = 2\cos^{-1}\left(\cos\left(\frac{\Delta\theta}{2}\right)\cos\left(\frac{\Delta\psi}{2}\right)\right) \tag{6}$$

$$d_{i,f} = \sin\phi\,\sin\left(\frac{\Delta\theta}{2}\right)\cos\left(\frac{\Delta\psi}{2}\right) - \cos\phi\,\sin\left(\frac{\Sigma\theta}{2}\right)\sin\left(\frac{\Delta\psi}{2}\right) \tag{7}$$

$$d_{j,f} = \cos\left(\frac{\Sigma\theta}{2}\right)\sin\left(\frac{\Delta\psi}{2}\right) \tag{8}$$

$$d_{k,f} = \cos\phi\,\sin\left(\frac{\Delta\theta}{2}\right)\cos\left(\frac{\Delta\psi}{2}\right) + \sin\phi\,\sin\left(\frac{\Sigma\theta}{2}\right)\sin\left(\frac{\Delta\psi}{2}\right) \tag{9}$$

where $\Delta\theta = \theta - \theta_f$, $\Sigma\theta = \theta + \theta_f$, $\Delta\psi = \psi - \psi_f$. By construction, α_f is independent of ϕ. Interestingly, eq 6 shows that α_f is also independent of the absolute orientations and only depends on the differences $\Delta\theta$ and $\Delta\psi$. The target orientation is an interpolation between $\vec{\mathbf{q}}_{\mathbf{f}}$ and $\vec{\mathbf{q}}$ through a rotation angle of $\Delta\alpha_f(= \alpha_f - \alpha_{0,f})$ about the same rotation axis, $\hat{\mathbf{r}}_{\mathbf{f}}$. As illustration, one instance of the feature orientation, $f = (111)$, is given by $\vec{\mathbf{q}}_{\mathbf{f}}\left(\phi, \cos^{-1}\frac{1}{\sqrt{3}}, \frac{\pi}{4}\right)$.

2.2.2. Symmetric Reduction. We also need to account for the redundancy associated with equivalent orientations in symmetric polyhedra. There exists a set of n_e rotations $E = \{\vec{\mathbf{e}}_i \mid i \in \{1, ..., n_e\}\}$, any of which, when applied to an arbitrary orientation $\vec{\mathbf{q}}$, generates an equivalent symmetry-preserving orientation. We do not consider chiral inversions to maintain handedness of the coordinate system. Using eq 6, the angle of closest approach can be formalized as

$$\alpha_{m,f}(\vec{\mathbf{q}}) = \min_{i\in\{1,\ldots,n_e\}} p(\vec{\mathbf{q}}\vec{\mathbf{e}}_i, \vec{\mathbf{q}}_{\mathbf{f}}) \tag{10}$$

For shapes with rotational chiral octahedral symmetries, there exist $(n_e =)$ 24 such equivalents for each orientation. For such cases, set E can be calculated as rotations to possible combinations of principal axes $6(+x, -x, +y, -y, +z, -z) \times 4(+y, -y, +z, -z) \times 1(+z, -z)$ from $(+x, +y, +z)$. Here, $+x$ refers to the positive direction of the global x-axis [typically $(1, 0, 0)$]. The function $\alpha_{m,f}$ has a lower bound of zero and an upper bound based on the rotation symmetry of the f^{th} feature. The upper bound for features $\{100\}$ and $\{111\}$ is $\max_{\forall(\theta,\psi)} \alpha_{m,\{100\}} = \max_{\forall(\theta,\psi)} \alpha_{m,\{111\}} = \cos^{-1}\frac{1}{\sqrt{3}} \approx 54.735°$, whereas for $\{110\}$, it is $\max_{\forall(\theta,\psi)} \alpha_{m,\{110\}} = \frac{\pi}{4}$. It is important to note that the reduction operation must be performed in the higher dimensional orientation space instead of the 2D projection space of θ and ψ. Although illustrated for the case of rotational octahedral symmetry, the formulation is generalizable to any symmetry.

In summary, for the current NP configuration $\vec{\mathbf{q}}(\phi, \theta, \psi)$, the following steps are performed for each relevant feature, f:

(a) Cylindrical symmetry of the interface: Factor out ϕ from $\vec{\mathbf{q}}$ to calculate the specific feature orientation $\vec{\mathbf{q}}_{\mathbf{f}}(\phi, \theta_f, \psi_f)$.
(b) Convert to a single rotation: Calculate the value of α_f and $\hat{r}_f$ from the rotation quaternion $\vec{\mathbf{d}}_f = \vec{\mathbf{q}}_{\mathbf{f}}\,\vec{\mathbf{q}}^{-1}$.
(c) Symmetric reduction: Repeat for all symmetric equivalents to get $\alpha_{m,f}$ and $\hat{\mathbf{r}}_{m,f}$.
(d) Biasing potential: Calculate $\Delta\alpha_{m,f} = \alpha_{m,f} - \alpha_{0,f}$ in radians and apply the bias $E_{t,f}$ as an equivalent torque about the corresponding axis $\hat{\mathbf{r}}_{m,f}$.

In the context of MD or Langevin dynamics, the above calculations are to be performed at each time step to ensure that torque is applied in the direction of closest approach to the equilibrium orientation. Effectively, the symmetric reduction operation ensures that each integration step includes a (greedy) gradient descent toward the nearest equilibrium orientation. Note that we have described here the method using the Euler angle representation for rotations for the sake of simplicity and to facilitate connections with previous work.[11,12] The method can also be implemented using a purely quaternion-based approach.

3. DISCUSSION

3.1. Comparison to Explicit-Solvent Calculations. The model, qualitatively and quantitatively, captures the behavior of an isolated NP at an explicit fluid−fluid interface. The Gaussian bias potential (eq 3b) is plotted for the RCO as a function of (θ, ψ) in Figure 1c. The relevant parameter set comprising the feature family $\{hkl\}$, spring constant $(k_{t,\{hkl\}})$, equilibrium angle

https://dx.doi.org/10.1021/acs.jctc.0c00283
J. Chem. Theory Comput. 2020, 16, 5866−5875

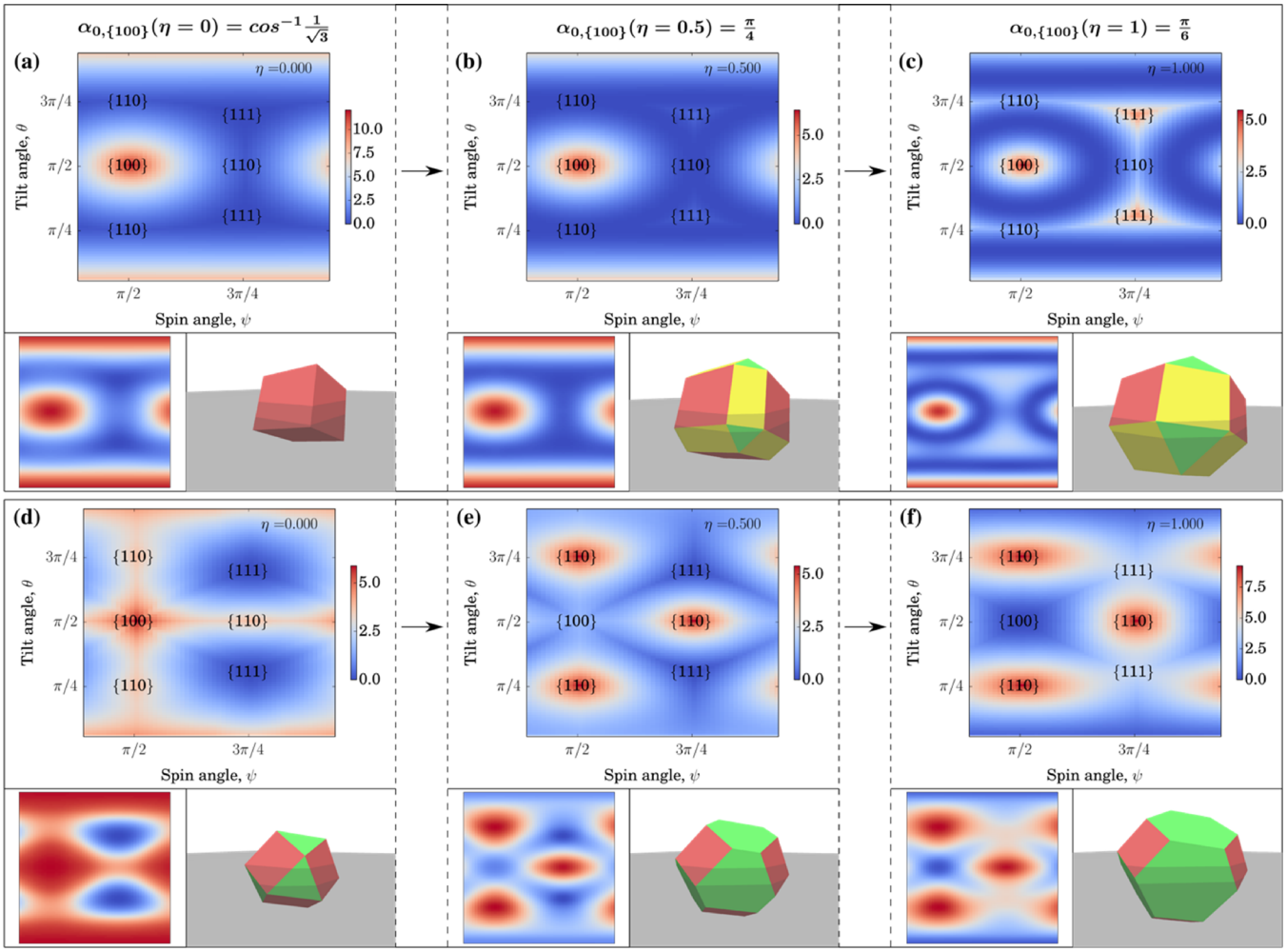

Figure 2. (a–c) Fitted bias PMF for representatives from the series of truncations from (a) CU (R^2 = 0.94) to (b) intermediate truncation of η = 0.5 (R^2 = 0.97) to (c) uniform RCO (R^2 = 0.50). The top panel shows the generated single-feature {100} harmonic bias potentials to be compared to the continuum model calculations (see main text) shown in the bottom left panel. The corresponding shapes at the interface are represented in bottom right panels. The red, green, and yellow facets correspond to the {100}, {111}, and {110} truncations. The effect of truncation is captured by the change in the equilibrium angle of approach $\alpha_{0,\{100\}}$. Due to the increased "roundedness" of the shape, both the FE and the bias potential become flatter. The same layout is followed for the series of {111} truncations from (d) CO (R^2 = 0.75) to (e) intermediate truncation of η = 0.5 (R^2 = 0.93) and finally to (f) uniform TO (R^2 = 0.82). The top panel in d–f represents the 2-feature [{111}, {110}] harmonic potential. The effect of truncation is seen to correlate with a switchover in dominance of specific features.

($\alpha_{0,\{hkl\}} \in [0, \max(\alpha_{m,f})]$), and potential well width parameter ($\sigma_{\{hkl\}}$) are presented in Table 1. The parameters were extracted by fitting the function E_t to the FE landscapes generated by explicit-solvent calculations (details in section II of the Supporting Information). Umbrella sampling (US)[20,21] calculations were performed (analogous to those for the explicit-solvent system in ref 11) for an isolated NP (with Langevin dynamics) to validate the implicit-solvent formulation.

In most cases, the effect of the interface, as it pertains to orientational behavior, is effectively captured by a single-feature potential. As expected, including a second feature leads to a better fit (Table 1) as seen in the increase in the corresponding coefficient of determination, R^2 values (details in section II of the Supporting Information). Moreover, using the Gaussian potential, with a well of finite depth(=ϵ_f) and width ($\sim\sigma_f$), achieves a higher level of fitness than that for the harmonic potential. The better fit is attributed to the finite nature of the Gaussian potential well, wherein the potential decays to zero at large angular differences ($E_{t,f} \to 0$ for $\Delta\alpha_{m,f} \gg \sigma_f$). In that regard, this form of E_t potential provides a more realistic description of the short-ranged physical biases associated with the NP facets. In contrast, the well depth/width imposed by a harmonic potential is bounded by the limits of the $\alpha_{m,f}$ function. Note that for relatively small values of $\Delta\alpha_{m,f}$, eq 3b describes a shifted harmonic-like potential with an effective spring constant $k_{t,f}$.

$$E_{t,f} = -k_{t,f}\sigma_f^{\,2}\exp\left(\frac{-\Delta\alpha_{m,f}^{\,2}}{2\sigma_f^{\,2}}\right) = \underbrace{-k_{t,f}\sigma_f^{\,2}}_{Shift} + \underbrace{\frac{1}{2}k_{t,f}\Delta\alpha_{m,f}^{\,2}}_{Harmonic} + O(\Delta\alpha_{m,f}^{\,4}) \quad (11)$$

In principle, the harmonic potential could be improved and made closer to the Gaussian well by introducing a cutoff angle (3rd parameter) beyond which the potential plateaus.

3.2. Effect of Change in Shape. Because our framework encapsulates key mathematical symmetries of the physical system, it has the ability to capture a wide range of NP orientation behavior. Although generated empirically, the

https://dx.doi.org/10.1021/acs.jctc.0c00283
J. Chem. Theory Comput. 2020, 16, 5866–5875

biasing functions can reveal physical insights into the interplay of different feature effects that determine a final orientation preference. For this and the following section, we illustrate our calculations using the harmonic form of the orientational bias potential. Although the harmonic form is less accurate than the Gaussian model, this difference does not change the qualitative features of the results (and conclusions thereof) or the physical interpretation of the key parameters $k_{t,f}$ and $\alpha_{0,f}$; indeed, the Gaussian model simply represents a higher order of fit as per the analysis of eq 11.

Consider a general cantellated cube with {110} and {111} facets. The vertices are given by permutations of $(\pm(1 + \sqrt{2\eta}), \pm 1, \pm 1)$. The parameter $\eta \in [0,1]$ represents the series of truncations from a cube (at $\eta = 0$) to RCO ($\eta = 1$). Instead of using the computationally intensive explicit-solvent model, we use a continuum model formulation (details in section III of the Supporting Information) to explore the serial change in orientation preference from {111} (CU) to {110} to {1n0} (RCO). This continuum model was shown[11] to capture the explicit-solvent FE landscapes of model NPs nearly quantitatively. Using the harmonic form, we show that the bias function (Figure 2a−c, top panel and Figure S3a) reproduces the orientation characteristics of the entire series as predicted by the continuum model (bottom-left panel).

From a physical standpoint, the orientation preference originates, in part, from the tendency to reduce interfacial contact between the two immiscible fluids. The NP achieves this by maximizing its excluded volume from the interfacial mixing region (equivalently, reducing the projected area of contact). For a perfect cube, this tendency orients the {100} facets as far away from the vertical as possible ($\max_{\forall(\theta,\psi)} \alpha_{m,\{100\}} \approx 54.735°$). As the cube becomes more rounded (i.e., relatively low value of asphericity[22]), there is a corresponding decrease in this preference. The orientation preference of the entire series can be studied in terms of the {100} feature potential. With increasing η, the PMF [Figure 2, top panel] is reproduced by a corresponding continuous decrease in $\alpha_{0,\{100\}}(\eta)$ from 54.735 to 30°

$$E_t(\eta, \vec{\mathbf{q}}) = \frac{k_{t,\{100\}}}{2}(\alpha_{m,\{100\}}(\vec{\mathbf{q}}) - \alpha_{0,\{100\}}(\eta))^2 \quad (12)$$

Further, for a given NP volume, we expect an increase in roundedness (increase in asphericity) to lead to a flatter FE landscape. Here, flatness of a function can simply be defined in terms of the difference between its maximum and the minimum values in the domain. Indeed, the limiting behavior would correspond to a flat (no orientation preference) landscape for a spherical NP. The formulation captures this effect, consistent with the theoretical and solvent-explicit calculations. Mathematically, this originates from the bounds of $\alpha_m \in [0, 54.735°]$, wherein an intermediate value of $\alpha_0 (= 30°)$ leads to a flatter $(\alpha_m - \alpha_0(\eta))^2$ function as compared to the case with an extreme value of α_0 (0 or 54.7°). This implies that the $(\alpha_m - \alpha_0)^2$ function is roughly able to capture the effect of shape. The RCO surface plot in Figure 1a also illustrates that the regions of deviation correspond directly to the relevant features: the pointed {1n0} edges of the otherwise rounded particle contribute the most to the potential landscape minima (blue regions). Comparing directly to the continuum model, the parameter, $k_{t,f}$, captures the physical effect of the NP volume and the implicit interfacial properties (e.g., surface tension[6,7,10] or internal energy per unit volume of the mixing region[11]). The bigger the particle and/or lower the degree of miscibility between the two solvents, the higher the value of $k_{t,f}$ (or the well depth, ϵ_f for a Gaussian potential) and vice-versa. It can be shown, through a combination of analysis from the continuum model and explicit-solvent simulations using polybead NP surfaces, that the variations in FE with changes in NP size are accounted for by the polybead model (see details in section V of the Supporting Information). The polybead model, however, suffers from only being able to change the NP size in discrete steps (in increments of the bead diameter). This limitation could be circumvented by changing the level of detail (beads per unit length and/or bead diameter) at the expense of increased computational load.

Similarly, consider the series of {111} truncations [Figure 2d−f and Figure S3b] from CO (at $\eta = 0$) to TO ($\eta = 1$). The vertices are given by permutations of $(\pm(1 + \eta), \pm 1, \pm 1)$. The PMF of the series can be described by the $F_S = \{\{111\}, \{110\}\}$ feature subset (details in section III of the Supporting Information). For CO, the {111} feature potential ($E_{t,\{111\}}$) largely dominates the PMF landscape [$k_{t,\{111\}} = 12.3$ and $k_{t,\{110\}} = 5.4\frac{k_BT}{\text{rad}^2}$]. However, as the {111} truncation increases, the major deviations in the potential landscape are caused by the pointed edges {110}. This leads to a {110} feature-dominated landscape for high values of η. The spring constants for TO are $k_{t,\{111\}} = 7.2$, $k_{t,\{110\}} = 28.3\frac{k_BT}{\text{rad}^2}$. The goodness-of-fit, R^2, is reported for both series in the Supporting Information (Figure S3).

3.3. Self-Assembly. A hollow-core polybead model[11] is used here to describe the faceted NP. The various facet types ({100}, {110}, {111}) of the NPs can be tuned to encode the specific patchy behavior (see Figure 3). It is known that the ligand binding energy is facet-specific and increases in the order {100} < {110} < {111}; i.e., deprotection is fastest for the {100} facet.[4,23] Therefore, in this study, we allow inter-NP epitaxial connections through the {100} facets only. The interaction between the (red) beads of two {100} surfaces is defined by the cut and linearly shifted (12-6) Lennard-Jones potential, U_{LJ}

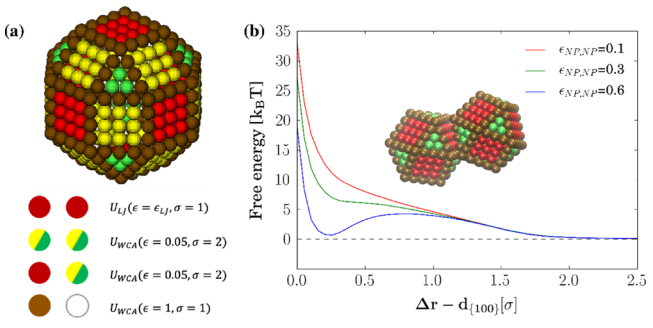

Figure 3. (a) Polybead representation of an RCO with an edge size of 5σ. Assuming fast desorption of ligands from the {100} facets, NPs are able to form epitaxial connections through the {100} facets (red beads) only. The {110} and {111} (yellow and green, respectively) facet beads are coarse-grained representations of the surface-bound ligands present on these surfaces. Therefore, these beads interact with the other facet-specific beads through a repulsive potential. The edge (brown) beads are modeled like hard-core beads. (b) FE plotted as a function of the distance between NP centers (Δr), shifted by the distance of closest approach along the {100}−{100} contact ($d_{\{100\}} = 5\sqrt{2}\sigma$ for a CO of edge $e = 5\sigma$). Increasing the inter-NP interaction parameter, $\epsilon_{\text{NP, NP}}$, leads to increased stability of the epitaxial connection.

https://dx.doi.org/10.1021/acs.jctc.0c00283
J. Chem. Theory Comput. 2020, 16, 5866−5875

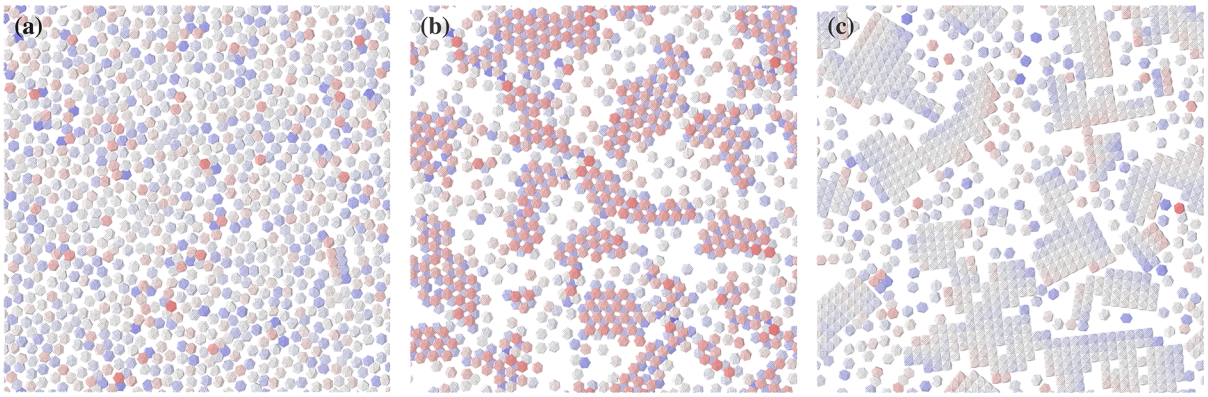

Figure 4. Assemblies of 1024 CO NPs at different interfacial conditions simulated with the solvent-implicit {111} harmonic bias. The particles are colored to reflect their vertical distance from the interface from out-of-plane (most red) to on-the−interfacial-plane (white) to into-the-plane (most blue). (a) Conditions corresponding to $k_v = 4\frac{k_BT}{\sigma^2}$ and $k_{t,\{111\}} = 25\,\frac{k_BT}{\mathrm{rad}^2}$ closely representing the explicit-solvent conditions. A strong {111} orientation preference coupled with a strong tendency to stay adsorbed to the interface leads to the formation of an unconnected monolayer. (b) Reduction in the vertical bias, $k_v = 2\frac{k_BT}{\sigma^2}$ and $k_{t,\{111\}} = 25\frac{k_BT}{\mathrm{rad}^2}$, facilitating the formation of small domains with a honeycomb bilayer structure. (c) For $k_v = 4\frac{k_BT}{\sigma^2}$ and $k_{t,\{111\}} = 12.5\frac{k_BT}{\mathrm{rad}^2}$, the system readily transforming into square monolayer clusters.

(cutoff radius, $r_{c,\,LJ} = 2.5\sigma$, $\sigma_{LJ} = \sigma$). The reduced units are quantified based on the physical properties of a representative solvent (see details in section IV of the Supporting Information) such that $\epsilon = 6.44 \times 10^{-21}$ J, $\sigma = 0.55$ nm, and $\tau = 2.7$ ps. The presence of stabilizing ligands bound to the {110} and {111} facets prevents inter-NP epitaxial connections from these surfaces. The steric interactions between ligand-covered surfaces of two NPs have been shown to be typically repulsive in nature.[24,25] Therefore, the beads belonging exclusively to the {110} and {111} (yellow and green, respectively) are coarse-grained to include the effect of the grafted ligands and interact with other facet-specific beads (yellow, green, and red) through a "bulky" and soft WCA-type repulsive potential[26] (with $\sigma_R = 2\sigma$, $\epsilon_R = 0.05\epsilon$, and truncated at $r = 2^{1/6}\sigma_R$). Since the edge (brown) beads can belong to multiple different facets, they are modeled as hard-core-like (non-overlapping) spheres to prevent ambiguous edge effects. The edge beads, therefore, interact with all other bead types using the WCA potential (with $\sigma_R = \sigma$, $\epsilon_R = \epsilon$, and truncated at $r = 2^{1/6}\sigma$).

We assume that the total PMF of an NP can be approximated as the additive contributions of the inter-NP interactions and the interfacial biases described in the previous sections. This assumption is justified by the fact that the biasing potentials, originating from the interactions between an isolated NP and the fluids, attempt to maximize the NP interfacial "footprint" to reduce the contact between the two immiscible fluids. These potentials hence primarily operate over the NP interfacial footprint and are, to the first approximation, independent from the inter-NP interactions, which primarily operate laterally, orthogonal to those footprints. Indeed, although NP−NP contacts alter the solvent environment between those contacts, the solvent environment normal to the NP footprint (which the biases primarily capture) should be similar to that experienced by an isolated NP.

The FE associated with the inter-NP distance is calculated (using umbrella sampling[20,21]) for different values of the Lennard-Jones interaction parameter, $\epsilon_{NP,NP}$. For this purpose, two CO NPs of edge $e = 5\sigma$ are simulated under the conditions predicted by the explicit-solvent simulations, i.e., $k_v = 4\frac{k_BT}{\sigma^2}$ and $k_{t,\{111\}} = 25\frac{k_BT}{\mathrm{rad}^2}$, leading to a {111} facet-up preference. As seen in Figure 3b, increasing the value of $\epsilon_{NP,NP}$ leads to formation and subsequent deepening of an FE well at a distance corresponding to the point of minimum energy (maximum stability) of epitaxial bonding between two {100} facets. The NPs, during their approach, need to overcome an FE barrier associated with two competing transformations: either (1) an orientation change from {111}-up to a {100}- or {110}-up or (2) a vertical shift away from the interfacial plane. This transformation is necessitated by the fact that the NPs in the {111}-up orientation do not have available {100} facets to bond along the interfacial plane.

Using a single-feature, harmonic {111} potential, we report the assembly of an array of 1024 CO NPs (of edge 5σ, i.e., a diameter of ∼5 nm) at three different interfacial conditions. The system is simulated in the NVT ensemble with the LAMMPS[27] package. Particle trajectories are integrated using Langevin dynamics to mimic the effect of Brownian diffusion in an implicit solvent. The simulations are performed with a time step of 13.5 fs (0.005τ), for a total of 135 ns. The Langevin thermostat maintains the temperature, T^*, at 0.85, with a relaxation time of approximately 27 ps. The cross section of the simulation box (parallel to the interface) has the dimensions $277\sigma \times 277\sigma$ (0.15 μm × 0.15 μm) with periodic boundaries across them. To mimic the gradual deprotection of the {100} facet, the inter-NP interaction parameter in U_{LJ} is ramped up from 0 to a final value of $\epsilon_{NP,\,NP}$, over the course of the simulation. For this case, we chose a sufficiently high $\epsilon_{NP,\,NP} = 0.6\epsilon$, to ultimately ensure irreversible bonding as can be seen in Figure 3b. At this value of $\epsilon_{NP,\,NP}$, the energy of interaction between two {100} facets at full contact is $-10\ k_BT$ or -0.5×10^{-19} J (see section V of the Supporting Information).

First, we simulate the conditions predicted by the explicit-solvent calculations, i.e., $k_v = 4\frac{k_BT}{\sigma^2}$ and $k_{t,\{111\}} = 25\,\frac{k_BT}{\mathrm{rad}^2}$. An unconnected monolayer is formed [Figure 4a] with a strong {111} preference characterized by an average value of (angle of closest approach) $\overline{\alpha}_{m,\,\{111\}} \approx 5°$. This is due to a relatively strong {111} orientation bias that prevents in-plane bonding, in tandem with a strong vertical bias that prevents out-of-plane movement. Lowering the vertical bias ($k_v = 2\frac{k_BT}{\sigma^2}$ and

https://dx.doi.org/10.1021/acs.jctc.0c00283
J. Chem. Theory Comput. 2020, 16, 5866−5875

$k_{t,\{111\}} = 25\frac{k_BT}{\text{rad}^2}$), facilitates out-of-plane inter-NP bonding. In this case, the system adopts a honeycomb bilayer configuration [Figure 4b], split into multiple smaller domains. The average value of the angle of closest approach is $\overline{\alpha}_{m,\{111\}} \approx 5°$. On the other hand, maintaining a high vertical bias while reducing the orientation bias ($k_v = 4\frac{k_BT}{\sigma^2}$ and $k_{t,\{111\}} = 12.5\frac{k_BT}{\text{rad}^2}$) leads to a prompt transformation into a square monolayer [Figure 4c], the structure that, given the conditions, expectedly maximizes inter-NP bonding. In this case, $\overline{\alpha}_{m,\{111\}} \approx 52°$, which is very far away from the equilibrium value ($\alpha_{0,\{111\}}$) of 0.

Both the honeycomb and the square superstructures have been reported extensively in experiments[7,15−18] and simulations[12] for nanocrystals of the lead chalcogenide (PbX) family. As discussed briefly in section 3.2, the changes in conditions (corresponding to theoretical parameters k_v, k_t, and $\varepsilon_{NP,NP}$) may be indirectly achieved experimentally by tuning a wide range of parameters such as the degree of miscibility of the two fluids, NP shape, NP surface chemistry, surface ligand chemistry, etc. We also note that $\alpha_{m,f}$ effectively embodies a single-valued measure of the orientation of the NP while being invariant to the rotational symmetries of the NP shape. This implies that it can function as an adequate local orientational order parameter (or be used as a parameter for a more complex one) for these symmetric polyhedral shapes.

4. CONCLUSIONS

The overarching goal of this study is to develop a tool for prediction of and control over the process of interfacial self-assembly of colloidal nanoparticles (NP) into epitaxially connected superlattices. We have developed an empirical model to augment the standard Brownian dynamics of an NP in a homogeneous fluid by including the effect of a planar fluid−fluid interface. By eliminating the need to simulate the solvent, we achieve a vast reduction in the number of particles to be simulated. This makes the simulation of a significant number of NPs (>1000) accessible for studies of phase behavior or nucleation. The proposed method potentially provides an efficient means to probe interfacial self-assembly to complement present experiments and guide future ones. We introduced the QOCO method to calculate the angle of closest approach (to NP facet orientation), a key geometrical metric to describe NP orientational behavior. This multistep method accounts for the cylindrical symmetry of the planar interface and the rotational symmetry of the particle shape, which ensure that the biasing potential is applied consistently across all equivalent features. We demonstrate the versatility of the formulation in capturing all major orientation characteristics for a wide range of shapes. The choice of feature space (F_S) encodes the information about the physical symmetry into the model. For some cases, a single-feature potential is sufficient to capture all the major orientation characteristics. However, depending on the level of required detail and complexity of the landscape, multiple features can be easily applied. In principle, the method is generalizable to any NP shape, and one could augment the (hkl) feature set to model more complex shapes and symmetries. Conversion to a quaternion-based formulation allows us to leverage the underlying symmetry in the orientational free-energy landscape to achieve an overall reduction in the number of independent torques applied by half. Also, independent controls on the vertical and orientation biases allow the description of a wide range of systems and conditions. The number of available degrees of freedom can be used to model fundamentally different interfacial conditions (i.e., fluid−NP and fluid−fluid surface tensions, NP size and shape, etc.).[11]

By studying the varying degrees of truncation for different NP shapes, we provide justification for our choice of linear combination of the feature potentials and a quadratic form of the feature potentials (eq 3). However, the form of the orientation bias is flexible and can be tuned to fit specific applications. We also investigated a three-parameter Gaussian bias potential (eq 3b). As seen in the corresponding R^2 values (Table 1 and section III of the Supporting Information), this form of the potential provides a considerable improvement over the harmonic form. From an empirical viewpoint, the $k_{t,f}$ parameter can be seen as a measure of the relative contribution of the f^{th} feature to the PMF landscape. However, we also show a strong physical correlation among $k_{t,f}$, the NP size, and interfacial properties. Similarly, we show that the chosen forms of the function and the feature choice combine to capture the effect of NP shape. Finally, we explored the deployment of our formulation in the context of the self-assembly of a large array of CO NPs. Our results show the existence of the honeycomb bilayer and the square monolayer at different interfacial conditions. These are consistent with the phases observed experimentally and reported in recent simulation studies. In this study, we have focused only on a specific case of NPs of size ∼5 nm. However, it is worth noting that the combined effect of the interplay of the orientation, vertical position preferences, and the energy of bonding can lead to vastly different phase behaviors for different NP sizes (see discussion in section V of the Supporting Information).

Rather than using analytical biasing potentials, the raw simulated FE landscape data could also be directly used (i.e., if stored as tables) and deployed in multi-NP simulations by employing a suitable tabular interpolation scheme (like piecewise cubic splines) to produce any required on-the-fly forces and torques. The quaternion-based functional fits advocated here, however, have the advantage of not only efficiently encapsulating the FE data (factoring out redundancies by incorporating the system's symmetries) and avoiding numerical discontinuities but also providing a deeper understanding of the behavioral trends with changes in particle shape or interfacial conditions through the concomitant trends in a few physically meaningful model parameters.

We observe that the degree of truncation introduces significant changes in the NP orientation preference. Ongoing simulations aim to collate and catalog the rich phase behavior of multi-NP systems as a function of the parameters controlling single-NP orientation preferences for different shapes. Within the scope of this study, we have not considered the effect on NP orientation of interactions of the NP surface or ligands with the fluids. However, it is straightforward to show that the proposed feature-based formulation can encode those characteristics too. Additional studies could also examine the self-assembly of a polydisperse mixture of similar shapes and sizes. Such efforts aim to achieve a better understanding of the actual physical conditions and processes accessible via experiments. As reported before,[11] as the NP moves away from the interfacial plane, the orientation preference changes; hence, an added layer of complexity would be to model the effect of change in orientation preference with changing distance from the interfacial plane (eq 2). Further, targeted studies are warranted to test and refine the assumption of additivity between inter-NP potentials and single-NP biases as employed in our multi-NP assembly simulations.

https://dx.doi.org/10.1021/acs.jctc.0c00283
J. Chem. Theory Comput. 2020, 16, 5866−5875

Finally, the NPs could be simulated with added coarse-grained ligand grafts to add a greater level of detail to the model.

■ ASSOCIATED CONTENT

Supporting Information

The Supporting Information is available free of charge at https://pubs.acs.org/doi/10.1021/acs.jctc.0c00283.

(Figure S1−S4) Technical details of quaternion-based orientational constraint, parameter fitting, goodness of fit for shapes of the truncated-cube family, mapping of physical units, and size scaling of the polybead model (PDF)

■ AUTHOR INFORMATION

Corresponding Author

F. A. Escobedo − *School of Chemical and Biomolecular Engineering, Cornell University, Ithaca, New York 14853, United States;* orcid.org/0000-0002-4722-9836; Email: fe13@cornell.edu

Author

U. Gupta − *School of Chemical and Biomolecular Engineering, Cornell University, Ithaca, New York 14853, United States*

Complete contact information is available at: https://pubs.acs.org/10.1021/acs.jctc.0c00283

Funding

The authors acknowledge funding support from NSF Grant CBET-1803878. This work used the Extreme Science and Engineering Discovery Environment (XSEDE), which is supported by National Science Foundation grant number ACI-1053575.

Notes

The authors declare no competing financial interest.

The core source-code files for QOCO in LAMMPS are freely available at https://github.com/escobedo-lab/USER-QOCO.git.

■ ACKNOWLEDGMENTS

The authors are grateful to Prof. T. Hanrath for useful exchanges.

■ ABBREVIATIONS

NP, nanoparticle; FE, free energy; PMF, potential-of-mean-force; QOCO, quaternion-based orientation constraint; CU, cube; CO, cuboctahedron; RCO, rhombicuboctahedron; TO, truncated octahedron; US, umbrella sampling; LJ, Lennard-Jones

■ REFERENCES

(1) Baumgardner, W. J.; Whitham, K.; Hanrath, T. Confined-but-Connected Quantum Solids via Controlled Ligand Displacement. *Nano Lett.* **2013**, *13*, 3225−3231.

(2) Kalesaki, E.; Evers, W. H.; Allan, G.; Vanmaekelbergh, D.; Delerue, C. Electronic Structure of Atomically Coherent Square Semiconductor Superlattices with Dimensionality Below Two. *Phys. Rev. B* **2013**, *88*, 115431.

(3) Savitzky, B. H.; Hovden, R.; Whitham, K.; Yang, J.; Wise, F.; Hanrath, T.; Kourkoutis, L. F. Propagation of Structural Disorder in Epitaxially Connected Quantum Dot Solids From Atomic to Micron Scale. *Nano Lett.* **2016**, *16*, 5714−5718.

(4) Whitham, K.; Hanrath, T. Formation of Epitaxially Connected Quantum Dot Solids: Nucleation and Coherent Phase Transition. *J. Phys. Chem. Lett.* **2017**, *8*, 2623−2628.

(5) Pieranski, P. Two-Dimensional Interfacial Colloidal Crystals. *Phys. Rev. Lett.* **1980**, *45*, 569−572.

(6) Morris, G.; Neethling, S. J.; Cilliers, J. J. A Model for Investigating the Behaviour of Non-Spherical Particles at Interfaces. *J. Colloid Interface Sci.* **2011**, 380.

(7) Evers, W. H.; Goris, B.; Bals, S.; Casavola, M.; de Graaf, J.; van Roij, R.; Dijkstra, M.; Vanmaekelbergh, D. Low-Dimensional Semiconductor Superlattices Formed by Geometric Control Over Nanocrystal Attachment. *Nano Lett.* **2013**, *13*, 2317−2323.

(8) van der Stam, W.; Gantapara, A. P.; Akkerman, Q. A.; Soligno, G.; Meeldijk, J. D.; van Roij, R.; Dijkstra, M.; de Mello Donega, C. Self-Assembly of Colloidal Hexagonal Bipyramid- and Bifrustum-Shaped ZnS Nanocrystals Into Two-Dimensional Superstructures. *Nano Lett.* **2014**, *14*, 1032−1037.

(9) Dasgupta, S.; Katava, M.; Faraj, M.; Auth, T.; Gompper, G. Capillary Assembly of Microscale Ellipsoidal, Cuboidal, and Spherical Particles at Interfaces. *Langmuir* **2014**, *30*, 11873−11882.

(10) Soligno, G.; Dijkstra, M.; van Roij, R. Self-Assembly of Cubes Into 2D Hexagonal and Honeycomb Lattices by Hexapolar Capillary Interactions. *Phys. Rev. Lett.* **2016**, *116*, 258001−258006.

(11) Gupta, U.; Hanrath, T.; Escobedo, F. A. Modeling the Orientational and Positional Behavior of Polyhedral Nanoparticles at Fluid-Fluid Interfaces. *Phys. Rev. Mater.* **2017**, *1*, No. 055602.

(12) Soligno, G.; Vanmaekelbergh, D. Understanding the Formation of PbSe Honeycomb Superstructures by Dynamics Simulations. *Phys. Rev. X* **2019**, *9*, No. 021015.

(13) Whitham, K.; Yang, J.; Savitzky, B. H.; Kourkoutis, L. F.; Wise, F.; Hanrath, T. Charge Transport and Localization in Atomically Coherent Quantum Dot Solids. *Nature Mater* **2016**, *15*, 557−563.

(14) Mitchell, E. E. L.; Rogers, A. E. Quaternion Parameters in the Simulation of a Spinning Rigid Body. *SIMULATION* **2016**, *4*, 390−396.

(15) Choi, J. J.; Bian, K.; Baumgardner, W. J.; Smilgies, D.-M.; Hanrath, T. Interface-Induced Nucleation, Orientational Alignment and Symmetry Transformations in Nanocube Superlattices. *Nano Lett.* **2012**, *12*, 4791−4798.

(16) Boneschanscher, M. P.; Evers, W. H.; Geuchies, J. J.; Altantzis, T.; Goris, B.; Rabouw, F. T.; van Rossum, S. A. P.; van der Zant, H. S. J.; Siebbeles, L. D. A.; Van Tendeloo, G.; Swart, I.; Hilhorst, J.; Petukhov, A. V.; Bals, S.; Vanmaekelbergh, D. Long-Range Orientation and Atomic Attachment of Nanocrystals in 2D Honeycomb Superlattices. *Science* **2014**, *344*, 1377−1380.

(17) van Overbeek, C.; Peters, J. L.; van Rossum, S. A. P.; Smits, M.; van Huis, M. A.; Vanmaekelbergh, D. Interfacial Self-Assembly and Oriented Attachment in the Family of PbX (X = S, Se, Te) Nanocrystals. *J. Phys. Chem. C* **2018**, *122*, 12464−12473.

(18) Peters, J. L.; Altantzis, T.; Lobato, I.; Jazi, M. A.; van Overbeek, C.; Bals, S.; Vanmaekelbergh, D.; Sinai, S. B. Mono- and Multilayer Silicene-Type Honeycomb Lattices by Oriented Attachment of PbSe Nanocrystals: Synthesis, Structural Characterization, and Analysis of the Disorder. *Chem. Mater.* **2018**, *30*, 4831−4837.

(19) Savoy, E. S.; Escobedo, F. A. Molecular Simulations of Wetting of a Rough Surface by an Oily Fluid: Effect of Topology, Chemistry, and Droplet Size on Wetting Transition Rates. *Langmuir* **2012**, *28*, 3412−3419.

(20) Torrie, G. M.; Valleau, J. P. Nonphysical Sampling Distributions in Monte Carlo Free-Energy Estimation: Umbrella Sampling. *J. Comput. Phys.* **1977**, *23*, 187−199.

(21) Kästner, J. Umbrella Sampling. *WIREs Comput. Mol. Sci.* **2011**, *1*, 932−942.

(22) Gantapara, A. P.; de Graaf, J.; van Roij, R.; Dijkstra, M. Phase Behavior of a Family of Truncated Hard Cubes. *J. Chem. Phys.* **2015**, *142*, No. 054904.

(23) Peters, J. L.; van den Bos, K. H. W.; Van Aert, S.; Goris, B.; Bals, S.; Vanmaekelbergh, D. Ligand-Induced Shape Transformation of PbSe Nanocrystals. *ACS Publ.* **2017**, DOI: 10.1021/acs.chemmater.7b01103.

(24) Kaushik, A. P.; Clancy, P. Explicit All-Atom Modeling of Realistically Sized Ligand-Capped Nanocrystals. *J. Chem. Phys.* **2012**, *136*, 114702.
(25) Fan, Z.; Society, M. G. J. O. T. A. C. Orientational Order in Self-Assembled Nanocrystal Superlattices. *ACS Publ.* **2019**, *141*, 1980−1988.
(26) Chandler, D.; Weeks, J. D.; Andersen, H. C. Waals Picture of Liquids, Solids, and Phase Transformations. *Science* **1983**, 787.
(27) Plimpton, S. Fast Parallel Algorithms for Short-Range Molecular Dynamics. *J. Comput. Phys.* **1995**, *117*, 1−19.

https://dx.doi.org/10.1021/acs.jctc.0c00283
J. Chem. Theory Comput. 2020, 16, 5866−5875